

Femtosecond laser bone ablation with a high repetition rate fiber laser source

Luke J. Mortensen,^{1,2} Clemens Alt,² Raphaël Turcotte,^{2,3} Marissa Masek,²
Tzu-Ming Liu,^{2,4} Daniel C. Côté,⁵ Chris Xu,⁶ Giuseppe Intini^{1,7,8,9} and Charles P. Lin^{2,7,9,*}

¹Department of Oral Medicine, Infection, and Immunity, Harvard School of Dental Medicine, Boston, Massachusetts, USA

²Advanced Microscopy Program, Center for Systems Biology and Wellman Center for Photomedicine, Massachusetts General Hospital, Harvard Medical School, Boston, Massachusetts, USA

³Department of Biomedical Engineering, Boston University, Boston, Massachusetts, USA

⁴Institute of Biomedical Engineering, National Taiwan University, Taipei, Taiwan

⁵Centre de Recherche Université Laval Robert-Giffard, Université Laval, Québec, QC G1J2G3, Canada

⁶School of Applied and Engineering Physics, Cornell University, Ithaca, New York, USA

⁷Harvard Stem Cell Institute, Cambridge, Massachusetts, USA

⁸Giuseppe_Intini@hsdm.harvard.edu

⁹Co-corresponding authors

*Charles_Lin@hms.harvard.edu

Abstract: Femtosecond laser pulses can be used to perform very precise cutting of material, including biological samples from subcellular organelles to large areas of bone, through plasma-mediated ablation. The use of a kilohertz regenerative amplifier is usually needed to obtain the pulse energy required for ablation. This work investigates a 5 megahertz compact fiber laser for near-video rate imaging and ablation in bone. After optimization of ablation efficiency and reduction in autofluorescence, the system is demonstrated for the in vivo study of bone regeneration. Image-guided creation of a bone defect and longitudinal evaluation of cellular injury response in the defect provides insight into the bone regeneration process.

©2014 Optical Society of America

OCIS codes: (170.1020) Ablation of tissue; (170.2520) Fluorescence microscopy; (060.4370) Nonlinear optics, fibers; (180.4315) Nonlinear microscopy.

References and links

1. A. Vogel, J. Noack, G. Hüttman, and G. Paltauf, "Mechanisms of femtosecond laser nanosurgery of cells and tissues," *Appl. Phys. B* **81**(8), 1015–1047 (2005).
2. A. Vogel, J. Noack, G. Hüttman, and G. Paltauf, "Femtosecond plasma-mediated nanosurgery of cells and tissues," in *Laser Ablation and its Applications* (Springer, 2007), pp. 231–280.
3. Y. Liu and M. Niemi, "Ablation of femoral bone with femtosecond laser pulses—a feasibility study," *Lasers Med. Sci.* **22**(3), 171–174 (2007).
4. B. Girard, D. Yu, M. R. Armstrong, B. C. Wilson, C. M. L. Clokie, and R. J. D. Miller, "Effects of femtosecond laser irradiation on osseous tissues," *Lasers Surg. Med.* **39**(3), 273–285 (2007).
5. D. C. Jeong, P. S. Tsai, and D. Kleinfeld, "All-optical osteotomy to create windows for transcranial imaging in mice," *Opt. Express* **21**(20), 23160–23168 (2013).
6. D. D. Lo, M. A. Mackanos, M. T. Chung, J. S. Hyun, D. T. Montoro, M. Grova, C. Liu, J. Wang, D. Palanker, A. J. Connolly, M. T. Longaker, C. H. Contag, and D. C. Wan, "Femtosecond plasma mediated laser ablation has advantages over mechanical osteotomy of cranial bone," *Lasers Surg. Med.* **44**(10), 805–814 (2012).
7. G. Nicolodelli, R. F. Lizarelli, and V. S. Bagnato, "Influence of effective number of pulses on the morphological structure of teeth and bovine femur after femtosecond laser ablation," *J. Biomed. Opt.* **17**(4), 048001 (2012).
8. J. Nguyen, J. Ferdman, M. Zhao, D. Huland, S. Saqqa, J. Ma, N. Nishimura, T. H. Schwartz, and C. B. Schaffer, "Sub-surface, micrometer-scale incisions produced in rodent cortex using tightly-focused femtosecond laser pulses," *Lasers Surg. Med.* **43**(5), 382–391 (2011).
9. K. Wang and C. Xu, "Tunable high-energy soliton pulse generation from a large-mode-area fiber and its application to third harmonic generation microscopy," *Appl. Phys. Lett.* **99**(7), 071112 (2011).
10. K. Wang, T. M. Liu, J. Wu, N. G. Horton, C. P. Lin, and C. Xu, "Three-color femtosecond source for simultaneous excitation of three fluorescent proteins in two-photon fluorescence microscopy," *Biomed. Opt. Express* **3**(9), 1972–1977 (2012).
11. N. G. Horton, K. Wang, D. Kobat, C. G. Clark, F. W. Wise, C. B. Schaffer, and C. Xu, "In vivo three-photon microscopy of subcortical structures within an intact mouse brain," *Nat. Photonics* **7**(3), 205–209 (2013).

12. O. Stachs, S. Schumacher, M. Hovakimyan, M. Fromm, A. Heisterkamp, H. Lubatschowski, and R. Guthoff, "Visualization of femtosecond laser pulse-induced microincisions inside crystalline lens tissue," *J. Cataract Refract. Surg.* **35**(11), 1979–1983 (2009).
13. M. S. Bello-Silva, M. Wehner, C. P. Eduardo, F. Lampert, R. Poprawe, M. Hermans, and M. Esteves-Oliveira, "Precise ablation of dental hard tissues with ultra-short pulsed lasers. Preliminary exploratory investigation on adequate laser parameters," *Lasers Med. Sci.* **28**(1), 171–184 (2013).
14. Z. Kalajzic, H. Li, L.-P. Wang, X. Jiang, K. Lamothe, D. J. Adams, H. L. Aguila, D. W. Rowe, and I. Kalajzic, "Use of an alpha-smooth muscle actin GFP reporter to identify an osteoprogenitor population," *Bone* **43**(3), 501–510 (2008).
15. L. J. Mortensen, C. E. Glazowski, J. M. Zavislan, and L. A. Delouise, "Near-IR fluorescence and reflectance confocal microscopy for imaging of quantum dots in mammalian skin," *Biomed. Opt. Express* **2**(6), 1610–1625 (2011).
16. I. Veilleux, J. A. Spencer, D. P. Biss, D. Cote, and C. P. Lin, "In Vivo Cell Tracking With Video Rate Multimodality Laser Scanning Microscopy," *IEEE J. Sel. Top. Quantum Electron.* **14**(1), 10–18 (2008).
17. X. Cai, Y. Lin, P. V. Hauschka, and B. E. Grottkau, "Adipose stem cells originate from perivascular cells," *Biol. Cell* **103**(9), 435–447 (2011).
18. A. Ludin, T. Itkin, S. Gur-Cohen, A. Mildner, E. Shezen, K. Golan, O. Kollet, A. Kalinkovich, Z. Porat, G. D'Uva, A. Schajnovitz, E. Voronov, D. A. Brenner, R. N. Apte, S. Jung, and T. Lapidot, "Monocytes-macrophages that express α -smooth muscle actin preserve primitive hematopoietic cells in the bone marrow," *Nat. Immunol.* **13**(11), 1072–1082 (2012).
19. J. A. Phillips, L. J. Mortensen, J. P. Ruiz, R. Sridharan, S. Kumar, M. Torres, P. Sharma, C. P. Lin, J. M. Karp, and P. V. Hauschka, "Advances in Single-cell Tracking of Mesenchymal Stem Cells (MSCs) During Musculoskeletal Regeneration," *Orthop. J. Harv. Med. Sch.* **14**, 22–28 (2012).
20. C. M. Cowan, Y.-Y. Shi, O. O. Aalami, Y.-F. Chou, C. Mari, R. Thomas, N. Quarto, C. H. Contag, B. Wu, and M. T. Longaker, "Adipose-derived adult stromal cells heal critical-size mouse calvarial defects," *Nat. Biotechnol.* **22**(5), 560–567 (2004).
21. B. J. Schaller, R. Gruber, H. A. Merten, T. Kruschat, H. Schliephake, M. Buchfelder, and H. C. Ludwig, "Piezoelectric bone surgery: a revolutionary technique for minimally invasive surgery in cranial base and spinal surgery? Technical note," *Neurosurgery* **57**, E410 (2005) (discussion).
22. K. Yoshida, K. Uoshima, K. Oda, and T. Maeda, "Influence of heat stress to matrix on bone formation," *Clin. Oral Implants Res.* **20**(8), 782–790 (2009).
23. A. P. Joglekar, H. Liu, G. J. Spooner, E. Meyhöfer, G. Mourou, and A. J. Hunt, "A study of the deterministic character of optical damage by femtosecond laser pulses and applications to nanomachining," *Appl. Phys. B* **77**, 25–30 (2003).
24. M. Lenzner, J. Krüger, S. Sartania, Z. Cheng, C. Spielmann, G. Mourou, W. Kautek, and F. Krausz, "Femtosecond Optical Breakdown in Dielectrics," *Phys. Rev. Lett.* **80**(18), 4076–4079 (1998).
25. A. Rosenfeld, M. Lorenz, R. Stojan, and D. Ashkenasi, "Ultrashort-laser-pulse damage threshold of transparent materials and the role of incubation," *Appl. Phys., A Mater. Sci. Process.* **69**(7), S373–S376 (1999).
26. A. Ben-Yakar and R. L. Byer, "Femtosecond laser ablation properties of borosilicate glass," *J. Appl. Phys.* **96**(9), 5316–5323 (2004).
27. D. Du, X. Liu, G. Korn, J. Squier, and G. Mourou, "Laser-induced breakdown by impact ionization in SiO₂ with pulse widths from 7 ns to 150 fs," *Appl. Phys. Lett.* **64**(23), 3071–3073 (1994).
28. J. Neev, L. B. Da Silva, M. D. Feit, M. D. Perry, A. M. Rubenchik, and B. C. Stuart, "Ultrashort pulse lasers for hard tissue ablation," *IEEE J. Sel. Top. Quantum Electron.* **2**(4), 790–800 (1996).
29. L. T. Canguero, R. Vilar, A. M. Botelho do Rego, and V. S. F. Muralha, "Femtosecond laser ablation of bovine cortical bone," *J. Biomed. Opt.* **17**(12), 125005 (2012).
30. J. Krüger, W. Kautek, and H. Newesely, "Femtosecond-pulse laser ablation of dental hydroxyapatite and single-crystalline fluoroapatite," *Appl. Phys., A Mater. Sci. Process.* **69**(7), S403–S407 (1999).
31. V. Wiegner, S. Zoppel, and E. Wintner, "Ultrashort pulse laser osteotomy," *Laser Phys.* **17**(4), 438–442 (2007).
32. S. Alves, V. Oliveira, and R. Vilar, "Femtosecond laser ablation of dentin," *J. Phys. D Appl. Phys.* **45**(24), 245401 (2012).
33. B. Emigh, R. An, E. M. Hsu, T. H. R. Crawford, H. K. Haugen, G. R. Wohl, J. E. Hayward, and Q. Fang, "Porcine cortical bone ablation by ultrashort pulsed laser irradiation," *J. Biomed. Opt.* **17**(2), 028001 (2012).
34. B. C. Stuart, M. D. Feit, A. M. Rubenchik, B. W. Shore, and M. D. Perry, "Laser-Induced Damage in Dielectrics with Nanosecond to Subpicosecond Pulses," *Phys. Rev. Lett.* **74**(12), 2248–2251 (1995).
35. B. M. Kim, M. D. Feit, A. M. Rubenchik, E. J. Joslin, P. M. Celliers, J. Eichler, and L. B. Da Silva, "Influence of pulse duration on ultrashort laser pulse ablation of biological tissues," *J. Biomed. Opt.* **6**(3), 332–338 (2001).
36. G. M. Rayan, D. T. Stanfield, S. Cahill, S. D. Kosanke, and J. A. Kopta, "Effects of rapid pulsed CO₂ laser beam on cortical bone in vivo," *Lasers Surg. Med.* **12**(6), 615–620 (1992).
37. J. S. Nelson, A. Orenstein, L.-H. L. Liaw, and M. W. Berns, "Mid-infrared erbium:YAG laser ablation of bone: The effect of laser osteotomy on bone healing," *Lasers Surg. Med.* **9**(4), 362–374 (1989).
38. A. Dela Rosa, A. V. Sarma, C. Q. Le, R. S. Jones, and D. Fried, "Peripheral thermal and mechanical damage to dentin with microsecond and sub-microsecond 9.6 microm, 2.79 microm, and 0.355 microm laser pulses," *Lasers Surg. Med.* **35**(3), 214–228 (2004).
39. B. Girard, M. Cloutier, D. J. Wilson, C. M. L. Clokie, R. J. D. Miller, and B. C. Wilson, "Microtomographic analysis of healing of femtosecond laser bone calvarial wounds compared to mechanical instruments in mice with and without application of BMP-7," *Lasers Surg. Med.* **39**(5), 458–467 (2007).

40. A. Vogel, N. Linz, S. Freidank, and G. Paltauf, "Femtosecond-Laser-Induced Nanocavitation in Water: Implications for Optical Breakdown Threshold and Cell Surgery," *Phys. Rev. Lett.* **100**(3), 038102 (2008).
41. V. Hovhannisyanyan, W. Lo, C. Hu, S.-J. Chen, and C. Y. Dong, "Dynamics of femtosecond laser photo-modification of collagen fibers," *Opt. Express* **16**(11), 7958–7968 (2008).
42. G. Latour, G. Georges, L. S. Lamoine, C. Deumié, J. Conrath, and L. Hoffart, "Human graft cornea and laser incisions imaging with micrometer scale resolution full-field optical coherence tomography," *J. Biomed. Opt.* **15**(5), 056006 (2010).
43. M. Han, L. Zickler, G. Giese, M. Walter, F. H. Loesel, and J. F. Bille, "Second-harmonic imaging of cornea after intrastromal femtosecond laser ablation," *J. Biomed. Opt.* **9**(4), 760–766 (2004).
44. V. Nuzzo, K. Plamann, M. Savoldelli, M. Merano, D. Donate, O. Albert, P. F. Gardezabal Rodriguez, G. Mourou, and J.-M. Legeais, "In situ monitoring of second-harmonic generation in human corneas to compensate for femtosecond laser pulse attenuation in keratoplasty," *J. Biomed. Opt.* **12**(6), 064032 (2007).
45. R. An, G. W. Khadar, E. I. Wilk, B. Emigh, H. K. Haugen, G. R. Wohl, B. Dunlop, M. Anvari, J. E. Hayward, and Q. Fang, "Ultrafast laser ablation and machining large-size structures on porcine bone," *J. Biomed. Opt.* **18**(7), 070504 (2013).
46. R. Orzekowsky-Schroeder, A. Klinger, S. Freidank, N. Linz, S. Eckert, G. Huttmann, A. Gebert, and A. Vogel, "Probing the immune and healing response of murine intestinal mucosa by time-lapse 2-photon microscopy of laser-induced lesions with real-time dosimetry," *Biomed. Opt. Express* **5**(10), 3521–3540 (2014).
47. M. F. Yanik, H. Cinar, H. N. Cinar, A. D. Chisholm, Y. Jin, and A. Ben-Yakar, "Neurosurgery: functional regeneration after laser axotomy," *Nature* **432**(7019), 822 (2004).
48. L. G. Ng, J. S. Qin, B. Roediger, Y. Wang, R. Jain, L. L. Cavanagh, A. L. Smith, C. A. Jones, M. de Veer, M. A. Grimbaldston, E. N. Meeusen, and W. Weninger, "Visualizing the neutrophil response to sterile tissue injury in mouse dermis reveals a three-phase cascade of events," *J. Invest. Dermatol.* **131**(10), 2058–2068 (2011).
49. D. Park, J. A. Spencer, B. I. Koh, T. Kobayashi, J. Fujisaki, T. L. Clemens, C. P. Lin, H. M. Kronenberg, and D. T. Scadden, "Endogenous bone marrow MSCs are dynamic, fate-restricted participants in bone maintenance and regeneration," *Cell Stem Cell* **10**(3), 259–272 (2012).
50. P. Bianco, X. Cao, P. S. Frenette, J. J. Mao, P. G. Robey, P. J. Simmons, and C.-Y. Wang, "The meaning, the sense and the significance: translating the science of mesenchymal stem cells into medicine," *Nat. Med.* **19**(1), 35–42 (2013).

1. Introduction

Multiphoton excitation and multi-harmonic generation with tightly focused femtosecond laser pulses have found widespread use in modern biological microscopy. Additional nonlinear optical effects such as multiphoton ionization and plasma formation can be induced when the laser pulse fluence is increased above the threshold for optical breakdown, resulting in local tissue damage or localized disruption. Properly controlled femtosecond laser pulses can generate extremely precise nanosurgical cuts in structures down to the subcellular level while maintaining cell viability [1, 2]. With repetitive pulsing and scanning, femtosecond lasers can also remove larger tissue volumes, such as ablation of hard tissues like bone (e.g. craniotomy or osteotomy) [3–7]. The rate of tissue removal depends on the fluence and the pulse repetition frequency. Most femtosecond ablation studies use an oscillator and regenerative amplifier configuration with output pulse repetition frequency in the kHz range. To increase the rate of tissue removal, the fluence can be increased beyond the ablation threshold [5–8]. However, increasing the fluence also runs the risk of increasing the zone of tissue damage, thus negating a major advantage of using femtosecond laser ablation, which is the precise spatial control afforded by a tightly focused beam at near-threshold fluences.

Here we describe laser ablation of bone using a compact turn-key fiber laser source with nanojoule pulse energies and near-threshold fluence at 5 MHz pulse repetition frequency. A similar laser source has been described for soliton generation, producing tunable near-infrared pulses suitable for multiphoton microscopy [9–11]. Compared to mode-locked Ti:sapphire lasers running at ~80 MHz, the relatively low pulse repetition rate in the MHz range of the fiber laser delivers higher pulse energy for similar average power levels, making it possible to ablate tissue without a separate amplifier [12, 13]. Here we use the doubled output (775 nm) of the 1550 nm fiber source for ablation and second harmonic generation (SHG) imaging, while simultaneously using the doubled output (960 nm) of a 1920 nm soliton generated with a photonic crystal large mode area fiber for imaging the green fluorescent protein (GFP) at a wavelength that is closer to the two-photon excitation maximum for the GFP. Both the ablating and the imaging beams are raster-scanned by a polygon-based scanner operating at near video-rate. The imaging acquisition pixel clock is synchronized to the 5 MHz laser output to yield exactly one pulse per pixel. We test this source for in vivo imaging and bone

ablation in a murine model of skeletal regeneration, using an alpha-smooth muscle actin transgenic mouse to visualize skeletal progenitor response [14] in laser created defects in the bone. The entire procedure is carried out under 1x PBS immersion so as to perform the ablation with two-photon imaging guidance (e.g. to visualize skeletal progenitor cells in the bone and use their location to guide ablation).

2. Experimental setup

The output from a compact turn-key 1550nm 5 MHz fiber laser pump source with 370 fs pulse width was split into two arms with a half-wave plate and a polarizing beam splitter (Fig. 1). One arm was frequency doubled to 775 nm using a 0.5 mm bismuth borate (BiBO) crystal (Newlight Photonics), which yielded a maximum pulse energy of 55-60 nJ at the manufacturer recommended maximum irradiance of 30 GW/cm². The polarization of the second arm was rotated using a half-wave plate, and coupled into an end-sealed polarization maintaining 35 μm core 1.43 meter large mode area single mode fiber with an effective mode area of 615 μm^2 (NKT Photonics). A coupling efficiency of 70% was attained (measured at 100 mW fiber input power). At 800 mW fiber input power a soliton was generated at 1920 nm via soliton self-frequency shift with 20-25 nJ pulse energy and 100 fs pulse width. The soliton was spectrally filtered using an 1800 nm long pass filter (Thorlabs) and frequency doubled with a second 0.5 mm BiBO crystal (Newlight Photonics), providing 10 nJ pulse energy at 960 nm. Each beam was recollimated and the two beams were combined using a 900 nm long pass filter (Thorlabs). The combined output beams were expanded before delivery to the imaging system so as to fill the objective back aperture (Fig. 1).

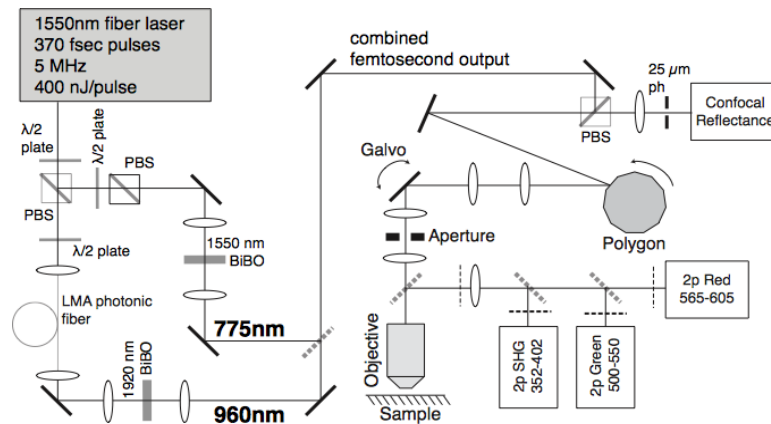


Fig. 1. System schematic. A 1550nm 5MHz fiber laser source simultaneously provides high power for doubling to 775nm using a bismuth borate crystal (BiBO) and feeds a large mode area (LMA) photonic crystal fiber to generate a 1920nm soliton for doubling to 960nm using a second BiBO. The power delivery to each arm is controlled by polarization using half wave plates and polarizing beam splitters (PBS). Imaging and ablation is performed using full field scanning, with an aperture in the intermediate image plane to modulate the area of ablation.

The imaging platform was modified from a previously described video rate scanner consisted of a spinning polygon for the fast (x) axis and a galvanometer for the slow (y) axis [15, 16]. After scanning, the beams were focused into the sample using a 60x water immersion objective with numerical aperture (NA) = 1.0 (Olympus). SHG of collagen was collected with a 377/50 nm bandpass filter (Semrock), green fluorescence with a 525/50 filter (Semrock), and red fluorescence/autofluorescence with a 585/40 filter (Semrock). A 775 nm confocal reflectance channel was set up using a polarizing beam splitter cube to separate the incident from the reflected light, which was detected using an avalanche photodiode module (Hamamatsu) placed behind a 50 mm focusing lens and a 25 μm pinhole (~1.0 Airy disk). All channels were digitized using the 5 MHz laser sync output as pixel clock, producing 500 x 500 pixel images at 15 frames per second with exactly one laser pulse per pixel. The delay

between the TTL laser sync output and the pixel clock input was experimentally adjusted based on maximized SHG signal to compensate for the difference in electrical vs. optical transit time. For ablation, the scan rate was slowed to 9 frames per second with the galvo angle adjusted to provide square pixels, which improved ablation versus 15 frames per second in preliminary testing. At this frame rate, the laser focus is scanned at a speed of 2.35 m/sec at the sample. Consecutive pulses arriving 200 nsec apart (5 MHz repetition rate) were displaced by $\sim 0.47 \mu\text{m}$, corresponding to 50% Airy disk overlap between pulses. To estimate the fluence, the diffraction limited spot size was used. The threshold for material removal (5 nJ, or 0.7 J/cm^2) was found to be independent of scanning speed when the scanning speed was set to 2.35, 5.7, and 11.4 m/s (displacement of the center of the laser focus by 0.47, 0.94, and $1.92 \mu\text{m}$ between consecutive pulses). However, in preliminary tests, 9 frames per second resulted in clean ablation craters whereas higher scanning speeds (larger interpulse spacing) sometimes produce uneven craters and premature termination of ablation. We therefore chose to perform ablation at 9 fps. To determine step size between planes, we tested $1.0 \mu\text{m}$, $0.5 \mu\text{m}$, $0.25 \mu\text{m}$, and $0.1 \mu\text{m}$ steps. We found that smaller step sizes ($0.25 \mu\text{m}$ or $0.1 \mu\text{m}$) yielded smooth crater walls whereas larger step sizes (0.5 or $1 \mu\text{m}$) leave some material behind. Since minimal difference between $0.25 \mu\text{m}$ or $0.1 \mu\text{m}$ steps was observed, $0.25 \mu\text{m}$ was chosen for subsequent experiments. To select the number of passes per plane, 1, 5, and 10 passes per plane were attempted and 10 passes per plane was found to produce the most complete material removal at each plane. As during imaging, the beam was raster scanned to remove material in 2 dimensions, with the sample axially translated for the third dimension using a computer controlled automated stage. An aperture was placed in the intermediate image plane to control the area of the ablated spot (Fig. 1). To remove bubbles and debris that could interfere with the ablation process, a flushing system was installed to move water or PBS across the sample.

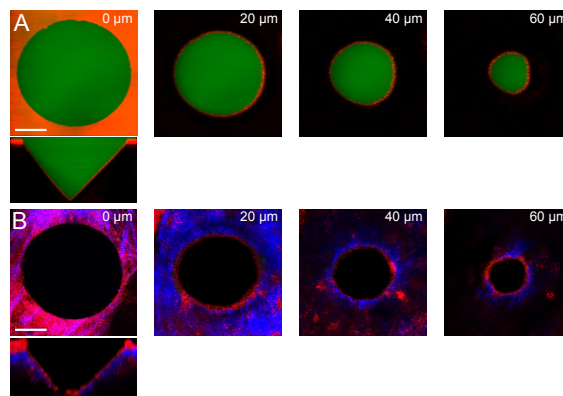


Fig. 2. Ablation in glass and ex vivo bone. Femtosecond laser ablation can effectively remove material in a homogenous material (A) like glass (green- dilute fluorescein solution, red-reflectance) or a heterogeneous medium (B) like ex vivo bone (blue- second harmonic generation, red- reflectance, green- autofluorescence, scale bar = $50 \mu\text{m}$).

3. Results

3.1 Preliminary ablation of glass and ex vivo bone

Our initial experiments were performed using a homogenous solid medium, a glass cover slip, by ablating under water immersion with a pulse energy found to effectively remove material (8 nJ pulse energy, fluence of $\sim 1.1 \text{ J/cm}^2/\text{pulse}$) and flushing at $\sim 15\text{-}20 \text{ mL/min}$ (Fig. 2(a)). After ablation, the immersion medium was changed to a dilute fluorescein solution (1 mg/mL) to assist with quantification of the removed volume of glass. Laser pulse energy was reduced to standard imaging levels ($\sim 2 \text{ nJ/pulse}$) and the scan rate increased to 15 fps. The dilute fluorescein solution could be easily imaged to the bottom of the defect, and the borders

matched well to those observed with the reflectance confocal channel (Fig. 2(a), Fig. 3 inset). A hole of around 70 μm depth was observed with a $\sim 120 \mu\text{m}$ opening at the top, defined by an aperture of fixed size placed in the intermediate image plane during ablation. The diameter of the hole decreased with depth until it terminated at about 70 μm below the glass surface (Fig. 2(a)).

Next we examined ex vivo bone ablation using the same parameters as above. A freshly excised skull was cleaned and mounted, and imaging and ablation performed immediately thereafter. With flushing, a hole of around 80 μm depth was attained with a similar cone shape as observed for glass (Fig. 2(b)). The edge of the hole was visualized by SHG signal and confirmed by reflectance confocal imaging (red signal), which enabled the depth of the hole to be quantified. These results indicate the potential of our approach to create and image locally confined defects in glass and calvarial mouse bone using a single laser source and scanning engine.

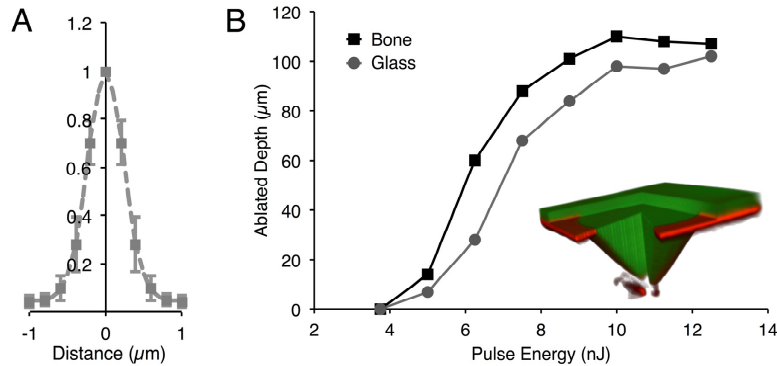


Fig. 3. Spot size and laser drilling efficiency dependence on pulse energy. (A) Average of Gaussian fit of 10 measured 0.1 μm radius 2-photon excited fluorescent beads. The $1/e^2$ radius is $0.48 \pm 0.09 \mu\text{m}$. (B) Glass and ex vivo bone exhibit similar thresholds for material removal (0.7 J/cm^2). The ablation depth increases between 0.7 and 1.4 J/cm^2 and plateaus thereafter, with minimal improvement using higher fluence. The ablation is performed using an aperture in the intermediate image plane that defines a $120 \mu\text{m}$ diameter ablation area at the sample. The ablated depth for each material is measured by the use of a dilute fluorescein solution in glass (3-D representation in inset) and confocal reflectance in bone.

3.2 Spot size and dependence of ablation depth on laser pulse fluence

The pulse energy should ideally be high enough above ablation threshold to ensure reproducibility from pulse to pulse, but not too far above the ablation threshold to minimize the risk of auxiliary damage. After scanning, the beams were focused into the sample using a 60x water immersion objective with numerical aperture (NA) = 1.0 (Olympus). The $1/e^2$ spot radius of the focused beam was estimated to be $0.47 \mu\text{m}$ based on diffraction limit and experimentally measured based on 2-photon-excited fluorescence of $0.1 \mu\text{m}$ radius fluorescent Tetraspeck beads (Invitrogen). The $1/e^2$ average Gaussian fit of 10 beads (Fig. 3(a)) was determined to be $0.48 \pm 0.09 \mu\text{m}$. Therefore, we used the diffraction limited spot size to calculate fluence throughout this work. To determine the threshold for glass and bone material removal by scanning ablation on our system, holes were drilled with a range of pulse energies at the sample and a surface diameter of $120 \mu\text{m}$ (Fig. 3(b)). To confine the ablated area, an aperture was placed in the intermediate image plane that imaged an open scan field of $120 \mu\text{m}$ diameter onto the sample surface. The sample was mounted on a computer-controlled translation stage and moved perpendicularly to the image plane during ablation. Subsequently, the ablation depth was measured by taking 3-D stacks using the confocal reflectance channel to visualize the crater. The depth measurement (in glass) was further confirmed by applying a dilute fluorescein solution to the immersion medium and acquiring 3D stacks of the fluorescence channel (Fig. 3(b), 3-D representation in inset). No material

removal occurred with 0.5 J/cm^2 fluence (3.75 nJ pulse energy) at the sample. The amount of material removed increased with increasing pulse fluence from 0.7 to 1.4 J/cm^2 ($5\text{--}10 \text{ nJ}$ pulse energy) for both bone and glass. Further increasing the pulse energy did not substantially alter the ablated depth for the chosen objective, the fixed size of the blocking aperture, and the tested range of pulse energies. The energy of 10 nJ/pulse was therefore used for subsequent experiments.

3.3 Autofluorescence reduction

One effect of the progressive hole termination that occurs with our high NA laser bone cutting is the non-ablative deposition of energy into the tissue surrounding the edges of the ablated defect, which can produce thermal damage and high levels of autofluorescence around the edges of the defect (Fig. 4(a)). The damaged tissue could potentially interfere with healing, and the autofluorescence could cause difficulty in evaluating the cellular response when GFP + cells need to be tracked in the presence of high autofluorescence background in the defect. To overcome this issue, we replaced the static mask in the intermediate image plane with a variable iris. As the ablation depth was increased, the iris opening was constricted at a rate matched to the frame rate (9 fps), number of passes (10), axial step size ($0.25 \mu\text{m}$), and NA of the objective (1.0) to yield a void volume with minimal edge autofluorescence (Fig. 4(b)). The resultant cone angle was $53 \pm 2^\circ$, which is slightly larger than the angle of an objective with NA = 1.0 with a $1\times$ PBS immersion medium (47°).

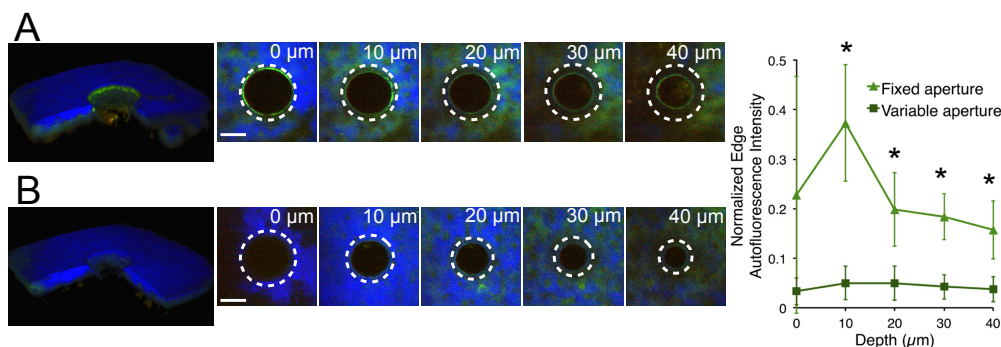


Fig. 4. Autofluorescence minimization. (A) When an aperture in the intermediate image plane of fixed size (open area inside the white dotted line) is used to limit the ablation area in bone, a significant amount of autofluorescence is observed around the edges of the defect when displayed in a 3 dimensional rendering or with progressive slices collected through the full thickness. With increasing depth, a reduction in size of the defect is observed. (B) With a variable aperture to match the angle of optimal ablation based on objective numerical aperture (white dotted line), less energy is deposited in the surrounding tissue so the amount of autofluorescence around the defect edges is greatly reduced. This trend is consistent when the average autofluorescence of a 5 pixel thickness ring around the defect edge is quantified at several discrete depths and normalized to the surface SHG intensity for defects drilled in $n = 3$ mice (* = $p < 0.05$, Students t-test with Bonferroni correction). Scale bar = $100 \mu\text{m}$.

3.4 In vivo bone defect generation and cellular response

After determining the optimal parameters for removal of ex vivo bone to generate a defect in the murine calvarial bone marrow cavity, we next investigated the potential of our system to generate and monitor a cellular response to a bone defect. For this purpose, alpha-smooth muscle actin green fluorescent protein (SMA-GFP) transgenic mice were used whose GFP expression in osteoprogenitor cells are strongly upregulated after bone injury [14]. The SMA-GFP is also expressed by adipose progenitor [17] and monocyte-macrophage [18] bone marrow cells. A laser defect was created in the mouse skull near SMA-GFP + cells in the bone marrow. To evaluate cellular response, the mouse was serially imaged on subsequent days using the doubled soliton wavelength of 960 nm to excite GFP (Fig. 5). Four sequential

imaging sessions are normally possible, limited by the build up of scar tissue and wear on the skin flap. Previous results indicate that a mechanical drill defect in the skull of a SMA-GFP mouse has a small number of SMA-GFP + cells that appear in a bone defect starting at 3 days after induction [19]. This time point was therefore chosen as the first follow-up, and a substantial infiltration of SMA-GFP + cells could be observed (Fig. 5). To exclude autofluorescent events, the red channel was simultaneously acquired. Yellow spots in the defect therefore indicate GFP- autofluorescent cells or debris. The cellular response in the defect increased at each time point up to 7 days after defect induction.

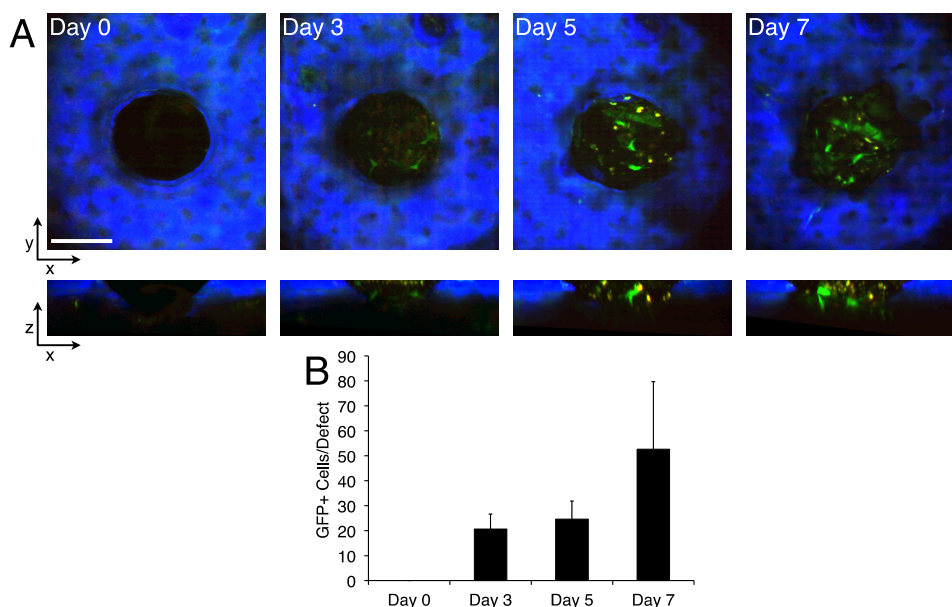


Fig. 5. Bone defect cell response. (A) α -smooth muscle actin GFP (SMA-GFP +) cells begin to appear in the laser defect by 3 days after defect induction. Cell number and intensity appear to increase 5 days later, and the defect is mostly filled with SMA-GFP + cells 7 days after (blue- second harmonic generation, red- autofluorescence, green- SMA-GFP + cells, scale bar = 100 μ m). (B) This trend is consistent when quantified over $n = 3$ defects.

4. Discussion

Advanced high power femtosecond lasers are a promising technology for the cutting of bone. They have been demonstrated to greatly reduce the peripheral damage that results from mechanical drilling techniques, which could be useful for applications ranging from clinical osteotomy and orthopedic drilling to in vivo brain imaging through thinned skull bone to the study of bone regeneration.

Bone cutting has standardly been performed using gross removal methods, such as mechanical drilling [6, 19, 20] or piezoelectric drilling [21]. However, the requisite mechanical force causes thermal damage and ejected debris that can slow healing [22]. In contrast, an ultrafast pulsed laser can be tightly focused to ablate tissue in a sub-micron space, and with scanning can remove large areas of material [5, 6]. With adequate pulse energy, the femtosecond pulses cause multiphoton ionization in the focal spot and transition into plasma, with a resultant bubble formation and collapse [2]. Femtosecond laser-induced multiphoton ionization, plasma formation, and cavitation bubble formation result in material removal at the laser focus, and the threshold fluence is reduced by orders of magnitude as compared to longer pulsed lasers [34]. The low threshold fluence reduces the total amount of energy deposited into the tissue, thereby minimizing both thermal damage and the size of the bubble that can extend the mechanical damage zone beyond the laser focus [34, 35]. Whereas longer pulsed lasers caused damage several cell diameters away from an ablated site [36–38],

femtosecond ablation has been found to only cause slight damage less than one cell diameter away [35]. In bone, femtosecond ablation in the near-IR has been investigated in a porcine femur model [3], has improved healing rates versus a mechanical drill in the mouse calvaria [39], and has demonstrated minimal thermal damage in the mouse calvaria [4]. Recently, femtosecond laser ablation has been investigated as a potential clinical technique for surgical osteotomy, where creation of a critically sized defect using an amplified 1 kHz source was found to reduce inflammatory damage and increase regeneration around the tissue edge as compared to a mechanically drilled defect [6]. Similarly, the bulk removal of bone with a KHz femtosecond pulsed amplified laser was used to allow in vivo brain imaging with a dynamic second harmonic generation feedback mechanism [5]. For all of these strategies, the imaging laser source was supplemented by an additional amplified high power kHz femtosecond laser.

As reviewed by Vogel and associates [1, 40], plasma mediated nano-cavitation is the dominant mechanism of tissue disruption by tightly focused femtosecond pulses for repetition rates up to ~1 MHz, whereas free-electron induced chemical decomposition is the dominant mechanism for repetition rates much greater than 1 MHz. The 5 MHz repetition rate of our fiber laser falls in between these two regimes, raising the question which mechanism drives tissue ablation. While we have not measured cavitation directly in our scanning setup, the fact that the laser spot is being scanned at a speed of 0.47 μm per 200 nsec (interval between laser pulses) suggests that the mechanism is most likely due to “single” pulse effects (i.e. laser-induced cavitation) rather than the cumulative effects of photochemical decomposition after many pulses ($>10^4$ pulses as typically used for laser microdissection with 80 MHz pulses, Table 2 in [1]). The threshold for material removal (0.7 J/cm²) is also in line with an optical breakdown-mediated mechanism. Furthermore, when femtosecond laser pulses are focused into pure water at a high numerical aperture, nanocavitation bubbles can be produced from thermoelastic tensile stress imparted at relatively low free electron density and threshold temperature (150-160°C). Whether such low density plasma-induced nanocavitation at the interface between tissue and the immersion liquid can effectively remove material remained to be explored.

Table 1. Femtosecond laser ablation thresholds for glass and bone. N.R. = not reported.

Reference	λ (nm)	Pulse duration (fs)	Repetition rate	# of pulses	Ablation threshold (J/cm ²)	Sample
Joglekar et al. [23]	527	600	228 Hz	1	7.67	Corning 0211 glass
Lenzner et al. [24]	780	220	1 KHz	50	3.5	Borosilicate glass
Rosenfeld et al. [25]	800	100	N.R.	20	0.9	Silicon dioxide
Ben-Yakar et al. [26]	780	200	N.R.	1	2.55 \pm 0.04	Borosilicate glass
Du et al. [27]	780	400	10 Hz	1	8	Silicon dioxide
Neev et al. [28]	1050	350	10 Hz	100	0.5	Human dentin
Cangueiro et al. [29]	1030	500	1 KHz	1	0.79 \pm 0.04	Bovine cortical bone
Kruger et al. [30]	615	300	3 Hz	100	0.6	Human enamel
Nicolodelli et al. [7]	800	70	1 KHz	10	0.6	Bovine femur
Wieger et al. [31]	1040	500	1 KHz	72.4	0.78	Bovine compact bone
Alves et al. [32]	1030	500	1 KHz	200	0.6 \pm 0.2	Human dentin
Girard et al. [4]	775	200	1 KHz	1000	0.69 \pm 0.08	Porcine cortical bone
Emigh et al. [33]	800	170	1 KHz	1	3.29 \pm 0.14	Porcine cortical bone
Bello-Silva et al. [13]	1045	500	100 KHz	40	1.6	Human enamel

The work presented herein takes advantage of a compact turn-key high power frequency doubled telecommunications fiber laser operating at MHz repetition rates with a soliton generating large mode area fiber to adjust available wavelengths. In addition to its promise in multi-color biological imaging [9–11], we have demonstrated that this laser provides adequate

power for direct ablation of bone at low MHz speeds without additional amplification. Due to its use in microfluidic and waveguide applications, femtosecond laser ablation of glass has been extensively investigated. The reported threshold values range from $\sim 8 \text{ J/cm}^2$ down to $\sim 0.9 \text{ J/cm}^2$ (Table 1). Similarly, published threshold values for bone ablation varied over almost an order of magnitude, from $\sim 3.3 \text{ J/cm}^2$ to 0.6 J/cm^2 . In general, our threshold values fall in the low end of the reported values for both glass and bone, however ablation threshold depends critically on both the focusing condition and the laser beam quality. In addition, our use of multiple passes for defect may explain the difference. A meaningful comparison with results from other studies is therefore not always possible because of differences in irradiation geometry, laser parameter, methods of estimating spot size and how the ablation threshold is determined.

A challenge of laser ablation to remove bone using a high NA imaging objective is that the high focusing angle yields a conical ablation crater. This is likely caused by clipping of the focused beam near the edge of the ablation crater, which would reduce the irradiance to below the ablation threshold and lead to the observed conical shape. The autofluorescence that occurred around the defect edges (Fig. 4(a)) is similar to the sub-ablation threshold photo-modification in type 1 collagen (which is the primary collagen component of bone) that results in increased autofluorescence and reduced SHG signal, as described by Hovhannisyan et al. [41]. By operating at a 5 MHz repetition rate, we were able to deliver nanojoule pulses at low average power and remove bone in a live mouse with precise control and minimal collateral damage as evidenced by the reduced autofluorescence around the ablation crater.

A consideration with ablation at a 5 MHz repetition rate is to provide adequate physical and temporal spacing between pulses in order to minimize the interaction between cavitation bubbles and subsequent laser pulses. The threshold bubble radius induced by 1024 nm, 340 fs pulses in water with an NA of 0.9 has been determined experimentally to be about $0.32 \mu\text{m}$ [40]. With a shorter wavelength (775 nm) and slightly higher NA (1.0) but longer pulse duration (370 fs), we expect comparable bubble size at threshold. In the scanning setup, the laser spot is displaced by a distance ($0.47 \mu\text{m}$) greater than the bubble radius. More importantly, the bubble will have collapsed before the arrival of the next laser pulse because the lifetime of such a small bubble ($\sim 25 \text{ ns}$) is much shorter than the time interval between laser pulses (200 ns at 5 MHz). It should be noted, however, that such small bubbles are produced in water at low plasma density, when thermalized electrons in the focal region generate a tensile stress that initiates phase transition by crossing the kinetic spinodal limit [1, 2]. At present, it is not known whether our scanning ablation at the interface between the immersion fluid and the glass and bone falls in the same regime as bubble formation in water near threshold. If higher plasma density is needed for material removal, then it is possible that the bubble radius and bubble lifetime can exceed the spatial and temporal spacing between laser pulses. If that is the case, either the repetition rate will need to be reduced, or the displacement between consecutive pulses will need to be increased (by increasing the scanning speed). In future work, it will be important to directly measure the bubble size and lifetime at the bone/water interface in order to further optimize the ablation scheme. In addition, experimentally we observe a necessity for flushing to remove coalescing bubbles and debris from the ablation site in glass and in bone. Without flushing, residual bubbles quickly build up and ablation ceases.

An important advancement in ablation of biological tissue has been the addition of imaging strategies to monitor femtosecond laser ablation immediately after or during the process. In the eye, optical coherence tomography [42] and SHG imaging [43] have been used to monitor femtosecond laser incisions in *ex vivo* corneas. In addition, SHG imaging has been used to correct for attenuation in the cornea, allowing for cutting at depth with minimal collateral damage [44]. In the bone, widefield microscopy has been used to evaluate defect size immediately after cutting [33, 45]. Further integration with SHG metrology has been allowed dynamic definition of a cutting path for femtosecond ablation [5]. The addition of similar strategies to our system could enable deeper cutting while minimizing collateral

damage. In addition there are numerous papers looking at cell response to laser-induced injury [46–48].

One application for in vivo laser cutting of bone is the study of cellular bone regeneration. Our system has allowed image-guided ablation and high resolution dynamic visualization of alpha-smooth muscle actin-GFP cells responding to the bone injury. We chose to focus on a population of in vivo bone repair cells suspected to be skeletal progenitor cells or mesenchymal stem cells (MSCs), which are precursors of structural components like osteoblasts or adipocytes [49, 50]. Since the absolute identity and function of skeletal progenitor cells in adult intramembranous bone remains elusive [50], the development of tools to dynamically study cell function in the canonical roles of maintenance and regeneration of bone is critical. Our results match well to the increase in SMA-GFP + cells found 7 days after osteoblast ablation using a chemically activated genetic approach by Kalajvic et al. [14], which provides support for the potential of our MHz ablation system as a tool for bone ablation in the study of important skeletal biology questions. When compared to results taken using a mechanical drill to create a calvarial defect and study bone regeneration [19], our femtosecond laser ablation offers precise control over defect depth, which ensures that SMA-GFP cells are supplied from the bone marrow rather than the dura mater. Our depth resolution could potentially find further use in the study of bone regeneration of a shallow defect that does not enter the bone marrow cavity, which might heal via a different mechanism.

5. Summary and conclusions

In this work, a fiber laser with soliton generation that is frequency doubled to 775nm and 960 nm provides ablation as well as imaging at 5 MHz. After determining the optimal ablation power and reducing autofluorescence, we performed in vivo removal of bone with the imaging scanning setup. When the frequency-doubled 775 nm source line was combined with reflectance confocal and a 960 nm fiber soliton doubled line for efficient excitation of GFP expressing cells, we generated a powerful system for the study of in vivo bone biology. In vivo laser ablation in the skull is a viable technique to enable image-guided generation of bone defects and the subsequent tracking of the defect healing response. The use of a single laser source and scanning system for imaging and ablation can simplify plasma ablation procedures and reduce the need for additional expensive, sensitive, and bulky amplifier modules. Additionally, the higher repetition rate as compared to regeneratively amplified Ti:Sapphire sources could potentially provide higher speed ablation of large areas in future work.

Acknowledgments

This work was supported by grants from the National Institutes of Health- NIH EB017274 to C. P. Lin and NIH/NIDCR DE021069 to G. Intini.